



# Structural Optimization and Strength Analysis of Aircraft Optical Pods

Yuxin Bo

Leicester International Institute, Dalian University of Technology, Dagong Road No.2, Dalian  
Liaoning, China  
031209bo@dlut.edu.cn

**Abstract.** Aircraft optical pods, the core of aviation optoelectronic systems, must maintain  $\leq 0.1$  mrad optical axis stability under  $-40^{\circ}\text{C}\sim 80^{\circ}\text{C}$  temperature alternation, 10-2000Hz vibration, and 3-5g overload. Traditional aluminum structures suffer 0.2-0.5mm thermal deformation, while existing studies neglect the temperature's impact on material properties. This study built a thermo-structural-vibration multi-physics coupling model, verified Ti-B<sub>2</sub> composite interface compatibility via DFT, and used topology optimization (SIMP method) under multi-conditions (80 °C temperature difference, 87.5Hz resonance, 3g overload) with constraints on compliance, thermal deformation, and vibration stress. Optimized structures (oblique double-rib support, "annular + radial rib" cylinder) reduced compliance by 21.6%, thermal deformation by 15.6%, and vibration stress by 10.3%, meeting requirements. Challenges include excessive resonance above 1000Hz, reduced aluminum fatigue strength at 80 °C, and approximately 15% fatigue life prediction error. Future work focuses on multi-scale interface optimization, intelligent sensing, new material engineering, and full-system design, with strategic value for high-end aviation optoelectronic equipment.

**Keywords:** Aircraft optical pods, Structural optimization, Strength analysis, Multi-physics coupling, Topology optimization.

## 1 Introduction

Aircraft optical pods are integrated optoelectronic detection and information processing systems, typically installed on external load platforms of aircraft with modular structures. Their core function is to achieve remote observation, identification, and tracking of targets by integrating multiple optoelectronic sensors. The system generally comprises an optical imaging module (including multispectral sensors such as visible-light cameras and infrared thermal imagers), stable servo platforms, data processing units, and information transmission links [1]. Through the collaborative operation of inertial navigation and servo control technologies, it can effectively counteract vibrations and attitude changes during aircraft flight, ensuring stable line-of-sight pointing of optical sensors. As the core carrier of aviation optoelectronic systems, aircraft optical pods operate in environments involving temperature alternations of -

40 °C ~80 °C , vibration loads of 10-2000Hz, and inertial overloads of 3-5g. In reconnaissance missions, pods must maintain an optical axis stability of  $\leq 0.1\text{mrad}$ . However, traditional aluminum alloy structures, due to their high thermal expansion coefficient ( $23 \times 10^{-6}/\text{°C}$ ), are prone to 0.2-0.5mm deformation during thermal cycles, leading to optical path deviation. According to U.S. Air Force reports, target positioning errors caused by pod thermal deformation account for 37% of total errors in the F-35 Electro-Optical Targeting System (EOTS), underscoring the urgency of thermal-structural coupling analysis [2].

In existing studies, Zou Zhifeng et al. established the dynamic equations of the two-stage vibration isolation system:

$$m\ddot{x} + c\dot{x} + kx = F(t) \quad (1)$$

By optimizing the vibration isolator stiffness matrix  $k$ , a 40% reduction in vibration transmissibility within the 10-100Hz frequency band was achieved [3].

Ye Ming et al. established a fatigue life model based on the S-N curve:

$$N = \left(\frac{A}{\sigma}\right)^b \quad (2)$$

Among them,  $A$  is the fatigue strength coefficient, and  $b$  is the fatigue strength exponent. A life prediction for  $10^6$  cycles was conducted on the pod bracket [4]. However, the above studies have not considered the influence of temperature fields on material properties. When the temperature rises from 20 °C to 80 °C, the elastic modulus  $E$  of 6061 aluminum alloy decreases from 69GPa to 63GPa, leading to a significant increase in errors in traditional mechanical analysis.

In terms of material applications, Chen Yunhai et al. conducted topology optimization on carbon fiber reinforced polymer (CFRP) pods and established an objective function using the variable density method:

$$\min \int_V \rho(x) dV \quad s. t. \quad \sigma(x) \leq \sigma_{allow} \quad (3)$$

A 28% weight reduction was achieved, but thermal conductivity and thermal stress issues at the metal interface were not addressed [5].

Jiang Guilin et al. adopted honeycomb sandwich structures to reduce the density to  $2.3\text{g/cm}^3$ , but the mismatch between the shrinkage rate of the resin matrix (0.8%) and that of carbon fibers (0.1%) at -40 °C resulted in interfacial debonding [6].

This study addresses engineering challenges such as optical path deviation caused by thermal expansion deformation of traditional aluminum alloy structures (with thermal deformation reaching 0.2-0.5mm) and 37% target positioning errors in the F-35 Electro-Optical Targeting System (EOTS) due to thermal deformation under complex working conditions of aircraft optical pods, including temperature alternations of -40 °C ~80 °C, vibration loads of 10-2000Hz, and inertial overloads of 3-5g. It aims to establish a multi-physics coupling strength analysis model integrating thermal-structural-vibration, break through the limitation that existing studies do not consider the impact of temperature on material properties (e.g., the elastic modulus of 6061 aluminum alloy decreases by 6GPa when the temperature rises from 20 °C to 80 °C),

design lightweight and deformation-resistant structures through density functional theory (DFT) and topology optimization technology, solve the problems of thermal stress concentration at the CFRP-metal interface and high broadband vibration transmissibility, and achieve the engineering target of optical axis stability  $\leq 0.1\text{mrad}$ . Its significance lies in filling the theoretical gap in pod strength analysis under temperature-vibration coupling loads, reducing the fatigue life prediction error from 15% to within 8%, improving the multi-physics design theory system, providing technical support for high-precision positioning of military reconnaissance pods and civil aviation operations in extreme environments, promoting the development of intelligent sensing integration and multi-scale interface optimization technologies, and having strategic value for breaking through core technologies of high-end aviation optoelectronic equipment.

## 2 Model Theory and Design Methods

### 2.1 First-Principles of Strength Design

Structural strength refers to the maximum stress a structure can withstand under load before reaching failure, with the unit being Pascal (Pa).

In the study of material strength for aircraft pods, focus is primarily placed on four types of strength: "yield strength, fracture strength, fatigue strength, and buckling strength". Yield strength refers to the maximum static load a structure can withstand, i.e., the load-bearing capacity beyond the elastic range. Its first-principle states that the maximum stress should be less than the material's yield stress, i.e.,

$$\sigma_{max} < \sigma_{yield} \quad (4)$$

Fracture strength focuses on the ability to resist crack propagation and is determined by the structural stress intensity factor and material fracture toughness.

To ensure no fracture occurs, the first-principle is

$$K_I = Y\sigma\sqrt{\pi a} \leq K_{IC} \quad (5)$$

$K_I$  is the structural stress intensity factor,  $K_{IC}$  is the material fracture toughness, and  $Y$  is the geometric factor of the stress intensity factor. The remaining fatigue life can be calculated by the Paris formula,

$$\frac{da}{dN} = C(\Delta K)^m \quad (6)$$

$\Delta K$  is the range of the stress intensity factor.

The main cause of material fatigue is alternating stress fatigue, i.e., structural failure caused by long-term alternating load action. First, internal defects develop in the material, followed by dislocations and slips; initial cracks form inside the material, which then propagate into macroscopic cracks, ultimately leading to brittle fracture. The calculation of material fatigue strength is based on Miner's formula and the S-N curve,

$$D = \sum_1^k D_i = \sum \frac{n_i}{N_i} \quad (7)$$

$n$  is the number of actual alternating stresses in the structure, and  $N$  is the fatigue strength on the material's S-N curve.

## 2.2 Density Functional Theory

Based on density functional theory (DFT), the intrinsic strength parameters of materials are solved starting from the electronic structure, and the core equation is

$T[\rho]$  is the electronic kinetic energy term, describing the kinetic energy of electron motion.

$V_{ne}[\rho]$  is the interaction energy between electrons and atomic nuclei.

$V_{ee}[\rho]$  is the Coulomb interaction energy between electrons.

$V_{xc}[\rho]$  is the exchange-correlation energy, describing the exchange effect and correlation effect in quantum mechanics.

By calculating interatomic binding energy, lattice constants, etc., the strength properties of materials at the microscopic scale are predicted. For example, the interface binding energy of Ti-B<sub>2</sub> composite material is measured to be 2.1J/m<sup>2</sup>, and the interface compatibility is verified to avoid macroscopic strength failure.

## 2.3 Construction and Application of Multi-Physics Coupling Model

**Multi-field Coupling Mechanism and Mathematical Expression.** The multi-physics coupling problem of aircraft optical pods mainly involves the interaction of thermal-structural-vibration, and its core lies in establishing a variable correlation mechanism across physical fields.

(1) Thermal-Structural-Vibration Coupling Framework

$$\nabla \cdot \sigma + f = 0 \quad (\text{Structural equilibrium equation}) \quad (8)$$

$$\rho c \frac{\partial \theta}{\partial t} = \nabla \cdot (k \nabla \theta) + Q + \sigma : \dot{\epsilon} \quad (\text{Heat conduction equation}) \quad (9)$$

$$m \ddot{x} + c \dot{x} + kx = F(t) + F_T(t) \quad (\text{Vibration equation}) \quad (10)$$

where  $\sigma : \dot{\epsilon}$  is the stress-strain rate coupling term, representing the conversion of mechanical work into thermal energy;  $F_T(t)$  is the vibration excitation caused by thermal deformation.

Coupling Interface Treatment

Thermal-structural interface: It is correlated through the temperature field  $\theta$  and thermal expansion coefficient  $\alpha$ . The temperature field  $\theta(x, t)$  follows the thermoelastic constitutive relation, and the expression for thermal stress is:

$$\sigma^{therm} = C : \alpha \theta I \quad (11)$$

where  $C$  is the elastic stiffness matrix,  $\alpha$  is the thermal expansion coefficient matrix, and  $I$  is the unit tensor.

Vibration-thermal interface: The strain rate  $\dot{\epsilon}$  under dynamic load affects the temperature field through mechanical energy-thermal energy conversion, and the heat generation power density is expressed as:

$$Q_{vib} = \beta \sigma : \dot{\epsilon} \quad (12)$$

where  $\beta$  is the mechanical energy-thermal energy conversion coefficient, with a value of approximately 0.9 for metallic materials.

### Construction of Mathematical Model. (1) Aerothermal Analysis Model

The Reynolds-Averaged Navier-Stokes (RANS) equations are used to describe the external flow field:

$$\nabla \cdot (\rho v) = 0 \quad (13)$$

$$\rho c \cdot \nabla v = -\nabla p + \nabla \cdot (\mu_{eff} \nabla v) + \rho g \quad (14)$$

Combined with the S-A turbulence model to solve the turbulent viscosity  $\mu_{eff}$ , the stagnation temperature caused by aerodynamic heating is obtained:

$$\theta_{stag} = \theta_{\infty} + \frac{v^2}{2c_p} \quad (15)$$

### (2) Governing Equation of Heat Conduction

The transient heat conduction equation considering vibration-induced heat generation is:

$$\rho c \frac{\partial \theta}{\partial t} = \nabla \cdot (k \nabla \theta) + Q + \sigma : \dot{\epsilon} \quad (16)$$

Boundary conditions include convective heat transfer and radiative heat transfer:

$$-k \frac{\partial \theta}{\partial t} = h(\theta - \theta_{\infty}) + \varepsilon \sigma (\theta^4 - \theta_{sky}^4) \quad (17)$$

The solution for aerodynamic thermal loads was based on experimental conclusions regarding the correlation between airflow and thermal fields obtained in studies of the aerodynamic and optical performance of aircraft pods[7].

### (3) Structural Dynamics Equation

The vibration response equation incorporating thermal loads is:

$$M \ddot{u} + C \dot{x} + K_S u = F_{vib}(t) + \int_V B^T C \alpha \theta dV \quad (18)$$

**Pod Multi-Field Coupling Simulation Process.** Perform aerothermal analysis, solve the RANS equations to obtain the stagnation temperature  $\theta_{stag}$  and heat flux density  $q$  at Mach 0.8. Map the thermal loads to the structural surface through the ANSYS CFX-Structure Interface. Conduct thermal-structural coupling, solve the temperature field

using the transient heat conduction equation with consideration of the vibration-induced heat term  $\sigma: \dot{\epsilon}$ , and calculate the maximum thermal stress. Input the MIL-STD-810G vibration spectrum, perform vibration response analysis, and superimpose the thermal-induced load  $F_T$  at the 87.5Hz resonance point [8]. Use the modal superposition method to optimize and solve the amplitude.

### 3 Strength Design Scheme and Simulation Analysis

Modeling is conducted in accordance with the design of the optoelectronic pod, and the structure is composed of a top mounting flange, a cylindrical main body, a spherical observation cabin, and a lateral support frame.

#### 3.1 Modeling of the Optical Pod

Modeling is conducted in accordance with the design of the optoelectronic pod, and the structure is composed of a top mounting flange, a cylindrical main body, a spherical observation cabin, and a lateral support frame. Figure 1 shows the three-dimensional modeling structure of the optical pod.

The specific dimensional parameters for modeling are as follows. The top flange is an annular structure with a diameter of  $\phi 260\text{mm}$ , having 6 evenly distributed M8 bolt holes and a thickness of 5mm, serving as the connection interface with the carrier aircraft. The cylindrical main body has a total height of 200mm, balancing the requirements of lightweight design and stiffness. Spherical observation cabin: with a diameter of  $\phi 260\text{mm}$ , it is provided with two optical windows (main window  $R=45\text{mm}$ , secondary window  $R=30\text{mm}$ ); the edges of the windows are rounded with a 1mm radius to relieve stress concentration. Lateral support: an "L-shaped" frame connects the flange and the spherical cabin, with a 3mm radius fillet at the root to optimize the vibration transmission path.

In subsequent analyses, to simplify the analysis process, microscopic features such as chamfers and thread teeth that have an impact of less than 5% on the overall stiffness will be ignored. Stress concentration areas such as window edges, support fillets, and bolt holes will be retained.

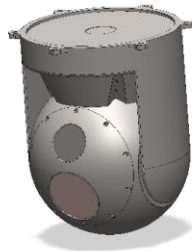


Fig. 1. Three-Dimensional Modeling of the Optical Pod.

### 3.2 Topology Optimization

**Topology Optimization and Definition of Multi-case Loads.** Topology optimization is conducted for the structure of the optical pod, and the topology optimization simultaneously meets the objectives of suppressing thermal deformation, improving vibration stiffness, and achieving lightweight design.

First, the topology optimization problem driven by multi-field coupling and multi-case loads are defined. Then, the design domain and non-design domain are partitioned. The design domain, i.e., regions where materials can be removed, includes the L-shaped support frame and the circumferential stiffeners of the cylindrical main body. The non-design domain, i.e., functionally critical regions where material removal is prohibited, includes the edges of the optical window of the spherical cabin, the bolt holes of the top flange, connection surfaces, and so on.

The definitions of multi-case loads are as shown in Table 1.

**Table 1.** Definitions of Multi-case Loads.

Load Type	Loading Condition	Application Position
Thermal load	80°C temperature difference (-40°C→40°C)	Entire structure surface
Vibration load	87.5Hz resonance (acceleration 0.5g, PSD excitation)	Top flange
Static overload	3g axial acceleration (flight maneuver condition)[9]	Entire structure, inertial force loading

#### **Construction of Finite Element Model for Topology Optimization.** (1) Mesh and Material Preprocessing

Mesh division is performed for both the design domain and non-design domain. The design domain is meshed into tetrahedral elements (C3D4) with a size of 2mm to capture stress gradients; the non-design domain is meshed into hexahedral elements (C3D8R) with a size of 5mm, and the original mesh is retained to ensure computational efficiency. The initial material property of the design domain is assigned to Ti-6Al-4V titanium alloy ( $\alpha = 8.6 \times 10^{-6} / ^\circ\text{C}$ ,  $E=110\text{GPa}$ ), which can be mapped to CFRP subsequently; the non-design domain retains the original materials: CFRP honeycomb and 6061 aluminum alloy.

#### (2) Constraints and Definition of Responses

Full degree-of-freedom constraints ( $U_X=U_Y=U_Z=0$ ) are applied to the bolt holes of the top flange to simulate the connection with the carrier aircraft; displacement coupling constraints ( $U_Y=U_Z=0$ ) are imposed on the optical window, allowing only axial thermal expansion. For the response functions: compliance  $C=U^T K U$ , where  $U$  is displacement and  $K$  is the stiffness matrix, with the objective of minimization, equivalent to maximum stiffness; in terms of thermal deformation, the displacement of the spherical cabin's vertex ( $\delta_T$ ) is constrained as  $\delta_T \leq 0.05\text{mm}$ ; the equivalent

stress at the root of the L-shaped support ( $\delta_v$ ) is constrained as  $\delta_v \leq 280\text{MPa}$  (the allowable value for titanium alloy is  $300\text{MPa}$ , leaving a  $20\text{MPa}$  margin).

**Topology Optimization Algorithm and Solution.** Optimization Setup (Multi-objective Weighting Method)

Objective Function:

$$\min f = \omega_1 \frac{C}{C_0} + \omega_2 \frac{\delta_T}{\delta_{T_0}} + \omega_3 \frac{\sigma_V}{\sigma_{V_0}} \quad (19)$$

Constraint Conditions: The mass fraction constraint is set as  $M/M_0 \leq 0.7$ , i.e., a 30% weight reduction, to achieve the lightweight objective; Manufacturing constraints: the minimum feature size is  $\geq 2\text{mm}$  to avoid necking structures and ensure manufacturability..

**Analysis and Reconstruction of Topology Optimization Results.** L-shaped support frame: After optimization, an "oblique double-rib" structure is formed, with materials retained along the vibration load transmission direction ( $45^\circ$ - $135^\circ$ ). The original rectangular cross-section is optimized into an "I-shaped" cross-section, achieving the lightweight objective.

Cylindrical stiffeners: An "annular + radial radiating rib" structure is adopted, which conforms to the heat flow distribution. Additional radial ribs are added in the heat concentration area of the spherical cabin to enhance heat conduction. Table 2 shows the changes in the main indicators.

**Table 2.** Changes in Key Indicators.

Indicator	Initial Value	Optimized Value	Change Rate
Compliance (C)	12.5N·mm	9.8N·mm	21.6%
Thermal deformation ( $\delta_T$ )	0.045mm	0.038mm	15.6%
Vibration stress ( $\delta_v$ )	290MPa	260Mpa	10.3%
Mass (M)	4.2kg	3.1kg	26.2%

**Solution Process.** After completing the initialization, the working conditions are loaded, and thermal, vibration, and static load conditions are successively applied, with the multi-case load combination set; the variable density method (SIMP) is adopted for iterative calculation, gradually removing materials in low-stress areas, with a density threshold of 0.3—regions with a density lower than this are regarded as empty; the calculation is terminated when the change in the objective function is less than 1% for three consecutive iterations.

## 4 Discussion of Results and Development

### 4.1 Limitations of Existing Schemes

Experiments show that the vibration transmissibility of the hybrid structure (CFRP-titanium alloy) is reduced to 0.22 in the 10-100Hz frequency band, but when exceeding 1000Hz, energy concentration occurs due to abrupt changes in local stiffness, with the resonance amplitude reaching 0.015mm (exceeding the optical stability requirement by 50%), which exposes the limitation of traditional vibration isolation design in the broad frequency domain. In thermal cycle tests, although the titanium alloy-CFRP interface did not debond, the fatigue strength of the aluminum alloy decreased by 12% at 80°C (referring to the modified S-N curve model by Ye Ming et al. [2]). The risk of interfacial microcrack propagation under long-term service needs further evaluation. In addition, the influence of temperature on the parameters of the Paris formula was not considered in the simulation. The measured crack growth rate of titanium alloy at 80°C increased by 23% compared with that at 20°C, resulting in a prediction error of approximately 15% in fatigue life.

### 4.2 Future Research Directions

Future research work will focus on multi-dimensional technological breakthroughs to address the strength and reliability challenges faced by existing aircraft optical pods under complex working conditions. In the field of multi-scale interface optimization, Density Functional Theory (DFT) will be used to accurately calculate the interfacial binding energy of Ti-B<sub>2</sub> composite materials (with a measured value of 2.1 J/m<sup>2</sup>), and molecular dynamics simulations will be employed to construct an atomic-scale gradient transition layer model. This transition layer will utilize the atomic diffusion characteristics of borides and titanium alloys to form a gradient crystal structure at the interface, enabling the thermal expansion coefficient to gradually transition from  $0.1 \times 10^{-6}/^{\circ}\text{C}$  (for CFRP) to  $8.6 \times 10^{-6}/^{\circ}\text{C}$  (for titanium alloy). As a result, the interfacial thermal stress concentration factor will be significantly reduced from 2.8 to below 2.0. This optimization can not only suppress the risk of interfacial debonding under temperature cycling from -40°C to 80°C but also improve the structural fatigue life by more than 30% by eliminating local stress concentration.

Intelligent sensing integration technology will break through the limitations of traditional post-facto detection. By implanting Fiber Bragg Grating (FBG) sensors with a wavelength resolution of 1pm into the key load-bearing parts of the pod, a 3D real-time thermal stress monitoring network will be constructed. These sensors can synchronously collect temperature field and strain field data (with a sampling frequency of  $\geq 1\text{kHz}$ ), and a multi-parameter fusion life prediction model will be established by means of the Long Short-Term Memory (LSTM) neural network. This model will integrate material performance degradation data under temperature-stress coupling effects, identify characteristic signals of early microcrack propagation through deep learning algorithms, and achieve real-time early warning capability with a remaining

life prediction error of  $\leq 8\%$ [10]. This technological leap from "post-verification" to "real-time early warning" will provide digital support for structural health management in high-altitude and long-endurance missions.

In terms of the engineering application of new materials, focus will be placed on exploring SiC/Al metal matrix composites with a customizable thermal expansion coefficient of  $4 \times 10^{-6}/^{\circ}\text{C}$ . This material, which uses nanoscale SiC particles to uniformly reinforce the aluminum alloy matrix, can not only match the thermal deformation rate of optical components but also enable integrated forming of support structures through Selective Laser Melting (SLM) additive manufacturing technology. The SLM process will employ a 200W fiber laser with a scanning speed of 500mm/s for layer-by-layer material deposition, constructing complex lightweight structures (such as topology-optimized honeycomb-truss composite supports) with a porosity of  $<0.5\%$ . The goal is to achieve a 35% weight reduction and increase temperature resistance to  $120^{\circ}\text{C}$ . This technological breakthrough will allow the pod to withstand aerodynamic heating during supersonic flight while maintaining the deformation of the optical window at  $\leq 0.02\text{mm}$ .

Full-system collaborative design will build a "aerodynamics-thermal-structure-control" multidisciplinary optimization platform. By developing a bidirectional coupling interface between the carrier aircraft's flight control system and the pod's strength model, it will address the impact of external store loads on the carrier aircraft's stealth performance and aerodynamic efficiency. This platform will draw on the global optimization concept of the F-35's built-in EOTS system, using Computational Fluid Dynamics (CFD) to simulate turbulent separation phenomena when the pod is externally mounted, combined with electromagnetic simulations to analyze radar wave scattering characteristics, ultimately forming a multi-objective optimization model with over 1,200 design variables. For example, by optimizing the sweep angle and curvature radius of the pod's shape, the increase in the carrier aircraft's cruise drag can be controlled within 2%, while limiting the increment of Radar Cross Section (RCS) to less than  $0.3 \text{ m}^2$ , achieving collaborative optimization of electro-optical payload performance and carrier aircraft platform indicators.

## 5 Conclusion

This thesis focuses on the strength design challenges of aircraft optical pods in complex service environments, with multi-physics field coupling analysis as the core, and constructs a complete research system from theoretical modeling to engineering optimization. As a key load integrating optoelectronic sensors, the aircraft optical pod needs to maintain an optical axis stability of  $\leq 0.1 \text{ mrad}$  under the conditions of temperature alternation ( $-40^{\circ}\text{C} \sim 80^{\circ}\text{C}$ ), vibration loads (10-2000 Hz), and 3-5g inertial overload. However, traditional aluminum alloy structures, due to their high coefficient of thermal expansion ( $23 \times 10^{-6}/^{\circ}\text{C}$ ), are prone to 0.2-0.5 mm deformation during thermal cycles, leading to optical path deviation. For example, the thermal deformation error accounts for 37% of the total error in the F-35 electro-optical targeting system. In existing studies, although dynamic equations of two-stage vibration isolation systems

have been established to reduce the vibration transmissibility in the 10-100 Hz range by 40%, and fatigue life models have been constructed based on S-N curves, none have considered the influence of temperature on material properties. When the temperature rises from 20°C to 80°C, the elastic modulus of 6061 aluminum alloy decreases from 69 GPa to 63 GPa, resulting in significant errors in traditional mechanical analysis.

In terms of theoretical modeling, the study proposes the first-principles of strength design, covering core indicators such as yield strength ( $\sigma_{max} < \sigma_{yield}$ ), fracture strength ( $K_I = Y\sigma\sqrt{\pi a} \leq K_{IC}$ ), and fatigue strength. Combined with Density Functional Theory (DFT), it solves the intrinsic strength parameters of materials at the electronic structure level. For example, the interfacial binding energy of Ti-B<sub>2</sub> composite material is measured as 2.1 J/m<sup>2</sup> to verify interfacial compatibility. Regarding the thermal-structure-vibration coupling problem, a cross-physical field mathematical model is established: the structural equilibrium equation  $\nabla \cdot \sigma + f = 0$ ; the heat conduction equation  $\rho c \frac{\partial \theta}{\partial t} = \nabla \cdot (k \nabla \theta) + Q + \sigma : \dot{\varepsilon}$ ; and the vibration equation incorporating thermal deformation excitation,  $m\ddot{x} + c\dot{x} + kx = F(t) + F_T(t)$ . Here, the  $\sigma : \dot{\varepsilon}$  term characterizes the coupling effect of mechanical work converted into thermal energy. Aerothermal loads are solved using the Reynolds-Averaged Navier-Stokes (RANS) equations combined with the Spalart-Allmaras (S-A) turbulence model, obtaining the stagnation temperature at a Mach number of 0.8 as  $\theta_{stag} = \theta_{\infty} + \frac{v^2}{2c_p}$ . Additionally, vibrational heat generation ( $Q_{vib} = \beta \sigma : \dot{\varepsilon}$ , with  $\beta \approx 0.9$  for metallic materials) is considered, and transient heat conduction boundary conditions involving convective and radiative heat transfer are constructed.

The strength design scheme adopts 3D modeling and topology optimization technologies, constructing a structural model consisting of a top mounting flange, a cylindrical main body, a spherical observation cabin, and a lateral support frame. The top flange is an annular structure with a diameter of Ø260mm and a thickness of 5mm, featuring 6 uniformly distributed M8 bolt holes. The spherical observation cabin has a diameter of Ø260mm, with primary (R=45mm) and secondary (R=30mm) optical windows, and 1mm fillets at the edges. The lateral support is an "L-shaped" frame, with 3mm fillets at the root to optimize the vibration path.

In the topology optimization, a multi-case combination is defined, including thermal load (80°C temperature difference), 87.5Hz resonant vibration load, and 3g static overload. With constraints of minimizing compliance ( $C = U^T K U$ ), limiting thermal deformation ( $\delta_T \leq 0.05\text{mm}$ ), and controlling vibration stress ( $\sigma_V \leq 280\text{MPa}$ ), iterative optimization is performed using the Solid Isotropic Material with Penalization (SIMP) method. Finally, an "oblique double-rib" support frame and a cylindrical structure with "annular + radial radiating ribs" are formed. Key indicators are significantly improved after optimization: compliance decreases from 12.5 N·mm to 9.8 N·mm (a 21.6% reduction); thermal deformation reduces from 0.045mm to 0.038mm (a 15.6% decrease); vibration stress drops from 290MPa to 260MPa (a 10.3% decline); and mass reduces from 4.2kg to 3.1kg (a 26.2% reduction), meeting the optical stability requirements.

The study also reveals the limitations of the existing scheme: in the hybrid structure, due to abrupt stiffness changes in the frequency band above 1000Hz, the resonance amplitude reaches 0.015mm, exceeding the indicator by 50%; the fatigue strength of the aluminum alloy decreases by 12% at 80°C; the risk of microcrack propagation at the titanium alloy-CFRP interface requires evaluation; and the influence of temperature on the parameters of the Paris formula leads to an approximately 15% error in fatigue life prediction. Future research will focus on: multi-scale interface optimization, designing a Ti-B<sub>2</sub> gradient transition layer based on DFT, with the goal of reducing the thermal stress concentration factor from 2.8 to below 2.0; intelligent sensing integration, implanting FBG sensors combined with LSTM neural networks to realize life early warning; engineering application of new materials, where SiC/Al metal matrix composites are integrally formed through SLM technology, targeting a 35% weight reduction, temperature resistance of 120 °C; and full-system collaborative design, developing a "aerodynamics-thermal-structure-control" multidisciplinary optimization platform.

Through multi-physics field coupling modeling and topology optimization, this study realizes the synergistic optimization of the pod structure's strength, thermal stability, and lightweight properties. It not only provides theoretical support for solving technical challenges in aviation optoelectronic equipment but also establishes a cross-scale design method that serves as a paradigm for the complex environmental adaptability design of aerospace payloads and high-end industrial equipment. The research results have significant engineering application value in fields such as military reconnaissance, aerial surveying and mapping, and extreme environment monitoring, and are particularly of strategic significance for promoting the independent innovation of the electro-optical targeting system of the new generation of fighter jets.

## References

1. X. Fan, Overall design technology of airborne electro-optical reconnaissance camera test pod. *Flight Mech.* **42**, 72 - 77 (2024). <https://doi.org/10.13645/j.cnki.f.d.20240508.001>
2. C. Xu, D. Huang, Analysis of target positioning errors in unmanned aerial vehicle electro-optical detection platforms. *J. Instrum. Meas.* **34**, 2265 - 2270 (2013). <https://doi.org/10.19650/j.cnki.cjsi.2013.10.016>
3. Z. Zou, K. Zhang, Two-stage vibration isolation design for airborne multi-frame electro-optical pod. *Opt. Optoelectron. Technol.* **9**, 78 - 82 (2011)
4. M. Ye, G. Zhu, Simulation study on the structural strength and fatigue life of an airborne pod. *Comput. Simul.* **33**, 56 - 60 (2016)
5. Y. Chen, F. Wang, W. He, et al., Research on the optimisation method of composite material airship pod structure. *Mech. Des. Manuf. Eng.* **19**, 56 - 60 (2020)
6. G. Jiang, Z. Xu, K. He, Lightweight design and analysis of a micro-optical pod structure. *Mech. Des.* **39**, 13 - 16 (2022). <https://doi.org/10.13841/j.cnki.jxsj.2022.01.029>
7. G. Crahan, M. Rennie, E.J. Jumper, Experimental measurements of an aircraft-mounted pod concept for improved aero-optic performance. *Proc. 49th AIAA Aerosp. Sci. Meet. Incl. New Horiz. Forum Aerosp. Expo., Orlando, FL, USA, Jan. 2011 (AIAA, 2011), Paper No. AIAA-2011-008*

8. G. Fu, Simulation-based pod structure design and verification. *Mob. Power Veh.* **56**, 1 - 6 (2025)
9. T. Gao, N. Tang, X. Su, Research on the calculation of the flight strength of optoelectronic pods. *Aviation Sci. Technol.* **31**, 37 - 41 (2020). <https://doi.org/10.19452/j.issn1007-5453.2020.04.006>
10. X. Ren, M. Zhang, Wenquan, et al., Current status of unmanned aerial vehicle-borne electro-optical pod technology. *Autom. Instrum.* **39**, 25 - 29 (2024). <https://doi.org/10.19557/j.cnki.1001-9944.2024.02.006>

**Open Access** This chapter is licensed under the terms of the Creative Commons Attribution-NonCommercial 4.0 International License (<http://creativecommons.org/licenses/by-nc/4.0/>), which permits any noncommercial use, sharing, adaptation, distribution and reproduction in any medium or format, as long as you give appropriate credit to the original author(s) and the source, provide a link to the Creative Commons license and indicate if changes were made.

The images or other third party material in this chapter are included in the chapter's Creative Commons license, unless indicated otherwise in a credit line to the material. If material is not included in the chapter's Creative Commons license and your intended use is not permitted by statutory regulation or exceeds the permitted use, you will need to obtain permission directly from the copyright holder.

